Geophysical Research Letters

RESEARCH LETTER
10.1029/2024GL113798

Inner Magnetospheric Oxygen Torus Induced by Electromagnetic Ion Cyclotron Waves

Zhiyong Wu[1,2,3], **Zhenpeng Su**[1,2,3,4], **Huinan Zheng**[1,2,3], **and Yuming Wang**[1,2,3]

[1]National Key Laboratory of Deep Space Exploration/School of Earth and Space Sciences, University of Science and Technology of China, Hefei, China, [2]CAS Center for Excellence in Comparative Planetology/CAS Key Laboratory of Geospace Environment/Mengcheng National Geophysical Observatory, University of Science and Technology of China, Hefei, China, [3]Collaborative Innovation Center of Astronautical Science and Technology, Harbin, China, [4]State Key Laboratory of Lunar and Planetary Sciences, Macau University of Science and Technology, Macao, China

Key Points:

- A novel approach based on electromagnetic ion cyclotron (EMIC) waves is proposed to infer ion abundances in the inner magnetosphere
- A narrow oxygen torus is identified in the density dip of the noonside plasmaspheric boundary layer during a quiet period
- The oxygen torus formation is attributed to a sequence of energy and matter transfer processes related to EMIC waves

Supporting Information:

Supporting Information may be found in the online version of this article.

Correspondence to:

Z. Su,
szpe@mail.ustc.edu.cn

Citation:

Wu, Z., Su, Z., Zheng, H., & Wang, Y. (2025). Inner magnetospheric oxygen torus induced by electromagnetic ion cyclotron waves. *Geophysical Research Letters*, *52*, e2024GL113798. https://doi.org/10.1029/2024GL113798

Received 21 NOV 2024
Accepted 5 FEB 2025

Abstract Cold oxygen ions escaping from the ionosphere and temporarily trapped near the plasmapause form the oxygen torus. Mass-loading by these oxygen ions significantly affects magnetospheric plasma processes. However, due to the technical challenges in measuring cold oxygen ions and the limited spatial and temporal coverage of space missions within the magnetosphere-ionosphere coupling system, the generation mechanism of oxygen torus remains unclear. Here, we propose a novel approach to determine the ion abundances from the observable polarization and propagation characteristics of electromagnetic ion cyclotron (EMIC) waves and identify a narrow oxygen torus near the noonside plasmapause during a geomagnetically quiet period. Our data and theoretical calculations suggest that the formation of this oxygen torus involved excitation of EMIC waves by ring current protons, wave-driven Landau heating of plasmaspheric electrons, heat conduction from the magnetosphere to the ionosphere, and upwelling of ionospheric oxygen ions into the magnetosphere.

Plain Language Summary The Earth's plasmasphere serves as a large reservoir of cold electrons and ions that escape from the ionosphere. The outer region, enriched with oxygen ions, is known as the "oxygen torus." Although discovered in the 1980s, the mechanisms responsible for generating the oxygen torus have remained unclear. One challenge is the extremely low energy of oxygen ions, which makes them difficult to detect with typical plasma instruments. Another challenge is the limited spatial and temporal coverage of space missions within the magnetosphere-ionosphere coupling system. Here, we propose a novel approach to determine the ion abundances using the observable polarization and propagation characteristics of electromagnetic ion cyclotron (EMIC) waves. For an oxygen torus identified through this approach, we attribute its formation to the excitation of EMIC waves by ring current protons, followed by wave-driven Landau heating of plasmaspheric electrons, heat conduction by the electrons from the magnetosphere to the ionosphere, and finally, the upwelling of ionospheric oxygen ions into the magnetosphere.

1. Introduction

The Earth's plasmasphere serves as a vast reservoir of cold electrons and ions that escape from the ionosphere (Lemaire & Gringauz, 1998). Low-energy (0.1–10 eV) oxygen ions can become temporarily trapped in a toroidal region near the plasmapause, known as the "oxygen torus" (Chappell, 1982; Goldstein et al., 2018; Horwitz et al., 1984). These oxygen ions can circulate within the magnetosphere (Keika et al., 2013; Kronberg et al., 2014; Yau et al., 2012) and, through mass-loading, affect local plasma processes, such as magnetic reconnections at the magnetopause or magnetotail (Kronberg et al., 2014; Shay & Swisdak, 2004; Yu & Ridley, 2013), as well as the generation and propagation of low-frequency waves (Henning & Mace, 2014; Omidi et al., 2013; Takahashi et al., 2006; X. Yu et al., 2015; M. Zhu et al., 2021). Since the first discovery of the oxygen torus by Chappell (1982), its generation mechanisms have remained unclear.

One challenge is the extremely low energy of oxygen ions. Direct measurements of the oxygen torus were successfully made by the Retarding Ion Mass Spectrometer (RIMS; Chappell et al., 1981) onboard the Dynamics Explorer 1 (DE-1). After the DE-1 mission ended in 1989, ion mass spectrometers on subsequent space missions have normally been unable to measure these cold ions effectively. In recent decades, the location of the oxygen torus has been inferred using the magnetoseismology technique (Fraser et al., 2005; Nosé et al., 2015, 2018; Takahashi et al., 2006), which involves determining the average ion mass from the measured eigenfrequencies of

standing Alfvén waves on closed field lines. However, this technique (Takahashi et al., 2015) cannot differentiate the abundances of different ions and, due to the regional distribution of waves, cannot provide a comprehensive view of the spatiotemporal morphology of the oxygen torus.

Another challenge is the large-scale magnetosphere-ionosphere coupling. The enrichment of oxygen ions in the inner magnetosphere indicates enhanced escape of oxygen ions from the ionosphere, facilitated by increased energy input from the magnetosphere to the ionosphere. Such energy input is usually prominent during geomagnetic storms and substorms (Z. Chen et al., 2023; Hull et al., 2019; Roberts et al., 1987; Yau et al., 1985; Yau & André, 1997). Oxygen ions may either directly flow into the outer plasmasphere along the field lines (Z. Y. Liu & Zong, 2022; Nosé et al., 2022) or experience significant radial and azimuthal cross-field transport before becoming trapped near the plasmapause (Nosé et al., 2015; Roberts et al., 1987). Given the limited spatial and temporal coverages of space missions, accurately identifying the generation mechanism of the oxygen torus has proven remarkably difficult.

In this letter, we propose a novel approach to determine the ion abundances from the observable polarization and propagation characteristics of electromagnetic ion cyclotron (EMIC) waves. EMIC waves have been frequently detected in the inner magnetosphere (e.g., Capannolo et al., 2019; Fraser et al., 1996; Horne & Thorne, 1990; S. Liu et al., 2019; Miyoshi et al., 2008; Morley et al., 2009; McCollough et al., 2009; Min et al., 2012; Meredith et al., 2014; Rauch & Roux, 1982; Usanova et al., 2012; Zhang et al., 2016; H. Zhu & Chen, 2019) and particularly within the oxygen torus (Nosé et al., 2020). The growth rate and cutoff frequency of EMIC waves have been shown to depend on the ion abundances (Miyoshi et al., 2019; Nosé et al., 2020; Omura et al., 2010). Using the newly developed approach, we identify a narrow oxygen torus near the noonside plasmapause during a quiescent period. Our analyses support the hypothesis that this oxygen torus resulted from the upwelling of oxygen ions from the ionosphere to the outer plasmasphere, facilitated by the magnetosphere-to-ionosphere energy transfer mediated by EMIC waves.

2. Observable Properties of EMIC Waves

On board the Van Allen Probes mission (Mauk et al., 2013), the Magnetometer (MAG) and the high frequency receiver (HFR) of the Electric and Magnetic Field Instrument and Integrated Science (EMFISIS) suite (Kletzing et al., 2013), and the Electric Field and Wave (EFW) instrument (Wygant et al., 2013) provided the data of magnetic fields of a 64 Hz sampling rate, densities (Kurth et al., 2015), and electric fields of a 32 Hz sampling rate. We resample the magnetic field vectors to a sampling rate of 32 Hz and estimate the spin-axis-aligned electric field component based on $\mathbf{E}\cdot\mathbf{B}=0$. We then apply a 1024-point Fast Fourier Transform with a 512-point overlap to the magnetic and electric field vectors of a 32 Hz sampling rate to generate the power spectral density matrices of waves. The wave normal angles and polarizations are determined by using the singular value decomposition technique on the magnetic power spectral density matrices (Santolík et al., 2002, 2003). The wave normal angle is defined as the angle between the wave vector and the background magnetic field. Based solely on magnetic field data, there is an inherent 180° uncertainty in determining the wave normal angle (Santolík et al., 2003). Polarization describes the characteristics of the wave's magnetic field in the plane perpendicular to the background magnetic field. Specifically, positive (negative) polarization occurs when the magnetic field rotates in a right-handed (left-handed) manner, and the amplitude of polarization is given by the ratio of the minor to the major axis of the wave magnetic field ellipse. The wave Poynting fluxes are calculated from the cross-power spectral density matrices (Santolík et al., 2010). The Poynting polar angle is defined as the angle between the Poynting flux and the background magnetic field.

From 6 to 12 February 2014, there were a series of weak geomagnetic storms and strong substorms (Figure 1a). The plasmasphere had undergone multiple cycles of erosion (down to $L<4$) and refilling (up to $L>6$) (Figure 1b). During a quiescent period from 05:20 UT to 06:05 UT on 13 February 2014, Van Allen Probe A observed the intense helium-band $\left(f_{cO}<f<f_{cHe}\right)$ EMIC waves near the noonside plasmapause at mid-latitudes ($\lambda\sim-17°$) in the southern hemisphere (Figures 1c and 1d). From the plasmaspheric boundary layer (05:20-05:29 UT) to the plasmaspheric core (05:29-05:58 UT), the wave power increased by approximately two orders of magnitude (Figures 1d and 1e). During this transition, the wave vector directions shifted from highly oblique directions $\left(\psi_k>50°\right)$ with respect to the background magnetic field to more field-aligned directions $\left(\psi_k<20°\right)$ (Figure 1f), and the wave polarizations reversed from positive to negative (Figure 1h). For all these EMIC waves, the Poynting fluxes were quasi-antiparallel $\left(\psi_P>160°\right)$ to the background magnetic field (Figure 1g), supporting

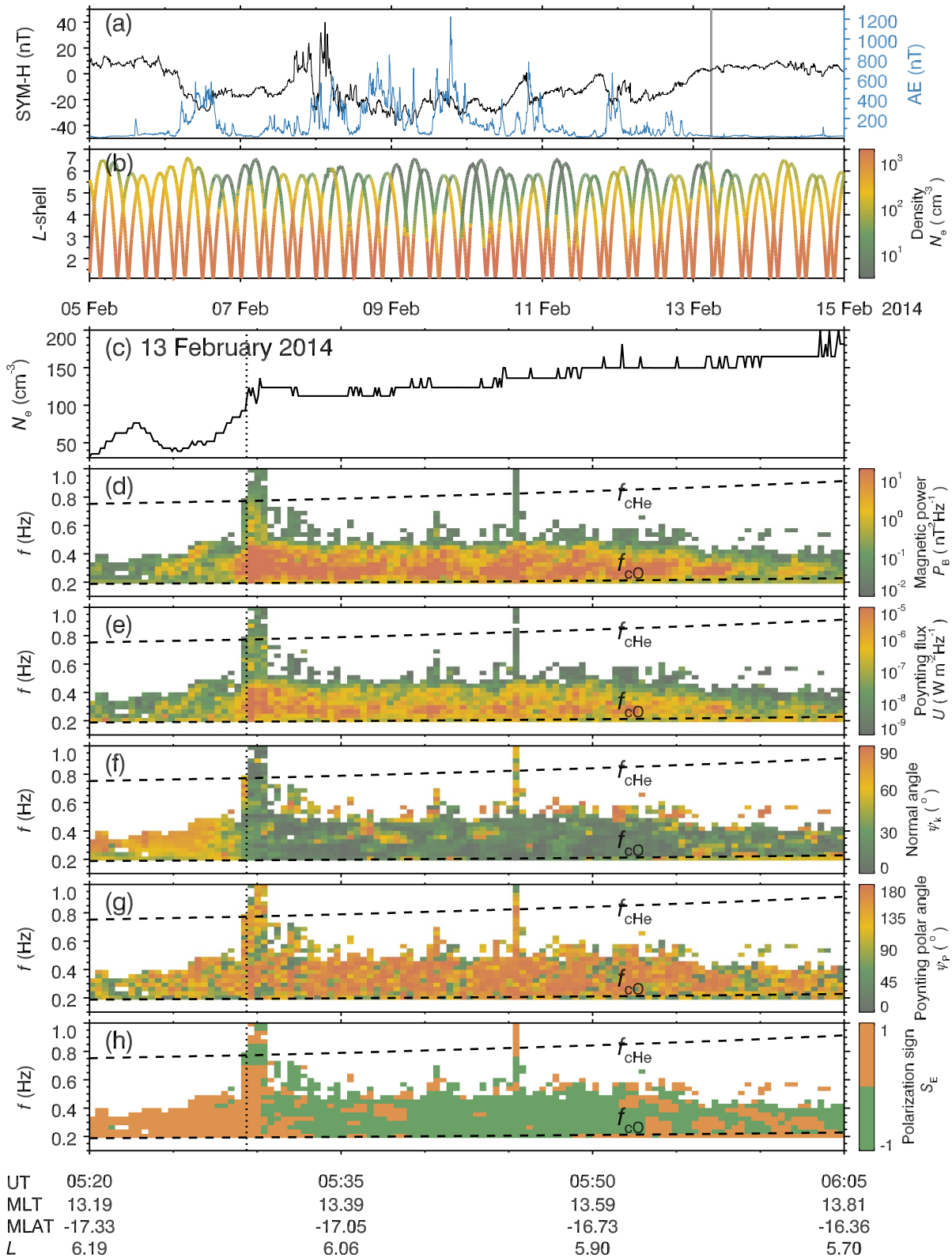

Figure 1.

that these waves were excited by energetic protons near geomagnetic equator (Cao et al., 2020; H. Chen et al., 2020; Horne & Thorne, 1993; Jordanova et al., 2008; N. Liu et al., 2020; Loto'Aniu et al., 2005; Teng et al., 2021; Xiao et al., 2007; Yin et al., 2022). Their frequency chirping characteristic indicates that EMIC waves experienced nonlinear amplification following a linear growth near the equator (An et al., 2024; Omura et al., 2010; Pickett et al., 2010; Shoji & Omura, 2011).

3. Inference of Ion Abundances From EMIC Waves

3.1. Fine Analysis of EMIC Waves

The instantaneous wave characteristics are derived from the magnetic field measurements taken at a sampling rate of 64 Hz. Field-aligned coordinates are defined as follows: $\hat{\mathbf{b}}$ is the unit vector along the background magnetic field $\mathbf{B}_0$ determined through a 1000-point moving average, $\hat{\mathbf{a}}$ is the unit vector pointing eastward, and $\hat{\mathbf{r}}$ completes the right-handed triad $\left(\hat{\mathbf{r}}, \hat{\mathbf{a}}, \hat{\mathbf{b}}\right)$. The magnetic fields of EMIC waves are obtained through an 80-point moving average minus a 320-point moving average. Within the time period between 05:20 UT and 06:05 UT, we select the data segments with regular sinusoidal waveforms. Each segment covers approximately one wave period, and its hodogram in the plane perpendicular to the background magnetic field is fitted to an ellipse using the Levenberg-Marquardt algorithm (Press, 2007). The hodogram gives the value of polarization, whose magnitude is defined as the ratio of the minor axis to the major axis of the fitted ellipse and whose sign is defined according to the rotating direction of the wave magnetic field with respect to the background magnetic field (positive for clockwise rotation and negative for anti-clockwise rotation). The instantaneous wave frequency is defined as

$$f = \frac{\Delta\phi}{2\pi\Delta t}, \tag{1}$$

where Δt is the duration of a data segment and $\Delta\phi$ is corresponding net change in the phase angle. Applying the minimum variance analysis technique (Sonnerup & Cahill, 1967) to a data segment gives the direction of wave vector $\hat{\mathbf{k}}$ and the wave normal angle

$$\psi_k = \arccos\left(\hat{\mathbf{k}} \cdot \hat{\mathbf{b}}\right). \tag{2}$$

3.2. Ion Species

Near the plasmaspheric boundary, the ion species may consist of H^+, He^+, O^+, and O^{++} (Chappell, 1982; Gallagher et al., 2016; Roberts et al., 1987). As shown in previous statistical studies (Gallagher et al., 2016; Roberts et al., 1987), O^{++} is observed more frequently in the late-evening sector, where the plasmasphere typically exhibits a bulge and intersects most intensely with the ring current. Although the exact cause remains unknown, a hypothesis suggests that the ring current heats the plasmasphere, enhancing the thermal diffusion of ionospheric ions, which theoretically favors the presence of O^{++} over O^+ (Chappell, 1982; Geiss & Young, 1981; Roberts et al., 1987; Young et al., 1977). For this specific event (Figure 1), the wave power, polarizations, and normal angles exhibited no observable changes near the O^{++} gyrofrequency (0.4 Hz), implying that O^{++} ions were probably quite sparse. Therefore, in the following analysis, we assume that only H^+, He^+, and O^+ exist. Their abundances $r_H = N_H/N_e$, $r_{He} = N_{He}/N_e$ and $r_O = N_O/N_e$ satisfy the charge neutrality condition

$$r_H + r_{He} + r_O = 1. \tag{3}$$

Figure 1. Overview of the EMIC wave event observed by Van Allen Probe A on 13 February 2014. (a) Geomagnetic indices SYM-H (black) and AE (blue) and (b) electron density N_e along the orbits of twin spacecraft of Van Allen Probes mission during 05–15 February 2014. The gray shading marks the time period from 05:20 to 06:05 UT on 13 February 2014. The following panels provide a zoomed-in view of the measurements taken by Van Allen Probe A during this interval. (c) Electron density N_e. (d) Magnetic power spectral density P_B. (e) Poynting flux U. (f) Wave normal angle ψ_k. (g) Poynting polar angle ψ_P. (h) The sign of polarization S_E. Positive (negative) values correspond to right (left)-hand polarized waves. In panels (c–h), the overlain vertical dotted lines mark the plasmapause. In panels (d–h), the overlain dashed lines are helium $\left(f_{cHe}\right)$ and oxygen $\left(f_{cO}\right)$ gyrofrequencies.

3.3. Polarization of EMIC Waves

We assume that the EMIC waves obey the cold plasma wave dispersion relation inside the high-density plasmasphere. Previous studies have found that when the temperatures of ions reach hundreds of eV, the EMIC wave dispersion relations can deviate significantly from the predictions of the cold plasma wave theory (L. Chen et al., 2013). For this specific event, the composition ratios of hot (>30 eV) ions were below 0.5% (Figure S1 in Supporting Information S1), which supports the validity of the cold plasma assumption. Given the background magnetic field strength B_0, the electron density N_e, the wave frequency f, and the wave normal angle ψ_k, the wave polarization E_B imposes the second constraint on the ion abundances. The magnetic polarization can be written as (Su et al., 2014; Tao & Bortnik, 2010)

$$E_B = \left[\frac{D\left(P - n^2 \sin^2\psi_k\right)}{P\left(n^2 - S\right)}\right]^{\sigma}, \tag{4}$$

with the parameter $\sigma = 1$ or -1 to ensure $|E_B| \le 1$, the wave refractive index n determined by the cold plasma wave dispersion relation

$$\tan^2\psi_k = -\frac{P\left(n^2 - R\right)\left(n^2 - L\right)}{\left(Sn^2 - RL\right)\left(n^2 - P\right)}, \tag{5}$$

and the notions R, L, D, S, and P of Stix (1962) depending on B_0, N_e, f and $(r_H,\ r_{He},\ r_O)$. Figure 2 gives two examples at 05:26:07 UT in the plasmaspheric boundary layer and at 05:40:22 UT in the plasmaspheric core. The local wave dispersion curves consist of two branches: Branch I and Branch II. At 05:26:07 UT with $B_0 = 200.1$ nT, $N_e = 51.9$ cm^{-3}, $f = 0.36$ Hz, $\psi_k = 70.3°$ and $E_B = 0.28$, the allowed values of O^+ abundance r_O range from 0 to 0.1 if the wave belongs to Branch I and from 0.12 to 0.4 if the wave belongs to Branch II. At 05:40:22 UT with $B_0 = 211.7$ nT, $N_e = 123.6$ cm^{-3}, $f = 0.27$ Hz, $\psi_k = 19.1°$ and $E_B = -0.30$, the allowed values of O^+ abundance r_O range from 0 to 0.05 if the wave belongs to Branch I and from 0 to 0.04 if the wave belongs to Branch II.

3.4. Propagation of EMIC Waves

The EMIC waves are generated near the geomagnetic equator by anisotropic energetic protons (Cao et al., 2020; H. Chen et al., 2020; Horne & Thorne, 1993; Jordanova et al., 2008; Loto'Aniu et al., 2005; N. Liu et al., 2020; Teng et al., 2021; Xiao et al., 2007; Yin et al., 2022). The wave growth rates typically peak at the parallel direction $(\psi_k = 0°)$ and have left-handed polarizations $(E_B < 0)$. The equatorial parallel wave branches I and II intersect with each other at the crossover frequency f_{cr} (Figure 3a). The left-handed polarized helium-band waves occur on Branch I between the cutoff frequency f_{ct} and the crossover frequency f_{cr}, and on Branch II between the crossover frequency f_{cr} and the helium gyrofrequency f_{cHe}. As these waves propagate away from the geomagnetic equator, their wave vectors deviate from the parallel direction due to the bending of magnetic field lines. For the obliquely-propagating EMIC waves, the dispersion branches I and II do not intersect with each other, and the linear mode conversion between Branch I and Branch II cannot occur (Horne & Miyoshi, 2016). In other words, without nonlinear effects, the EMIC waves persist on the same wave branch during their propagation from the geomagnetic equator to the observer.

These characteristic frequencies f_{ct}, f_{cr}, and f_{cHe} depend on the equatorial magnetic field B_{eq} and ion abundances. For this specific event, the background magnetic field can be well modeled as a dipole field (Figure 3b). The equatorial magnetic field strength is scaled from the observed magnetic field strength to $B_{eq} = B_0/\bar{B}$, with the scaling factor $\bar{B}$ determined under a dipole assumption. The ion abundances are assumed to be approximately constant from the equator to the observer. The dispersion branch invariance, that is, the waves always belonging to the same dispersion branch as they propagate from the equatorial source to the mid-latitude observer, imposes the third constraint on the ion abundances. Figures 3c and 3d present the analysis for the same data segments as Figures 2a and 2b. The O^+ abundance r_O is further restricted to 0.24–0.4 at 05:26:07 UT and 0–0.04 at 05:40:22 UT.

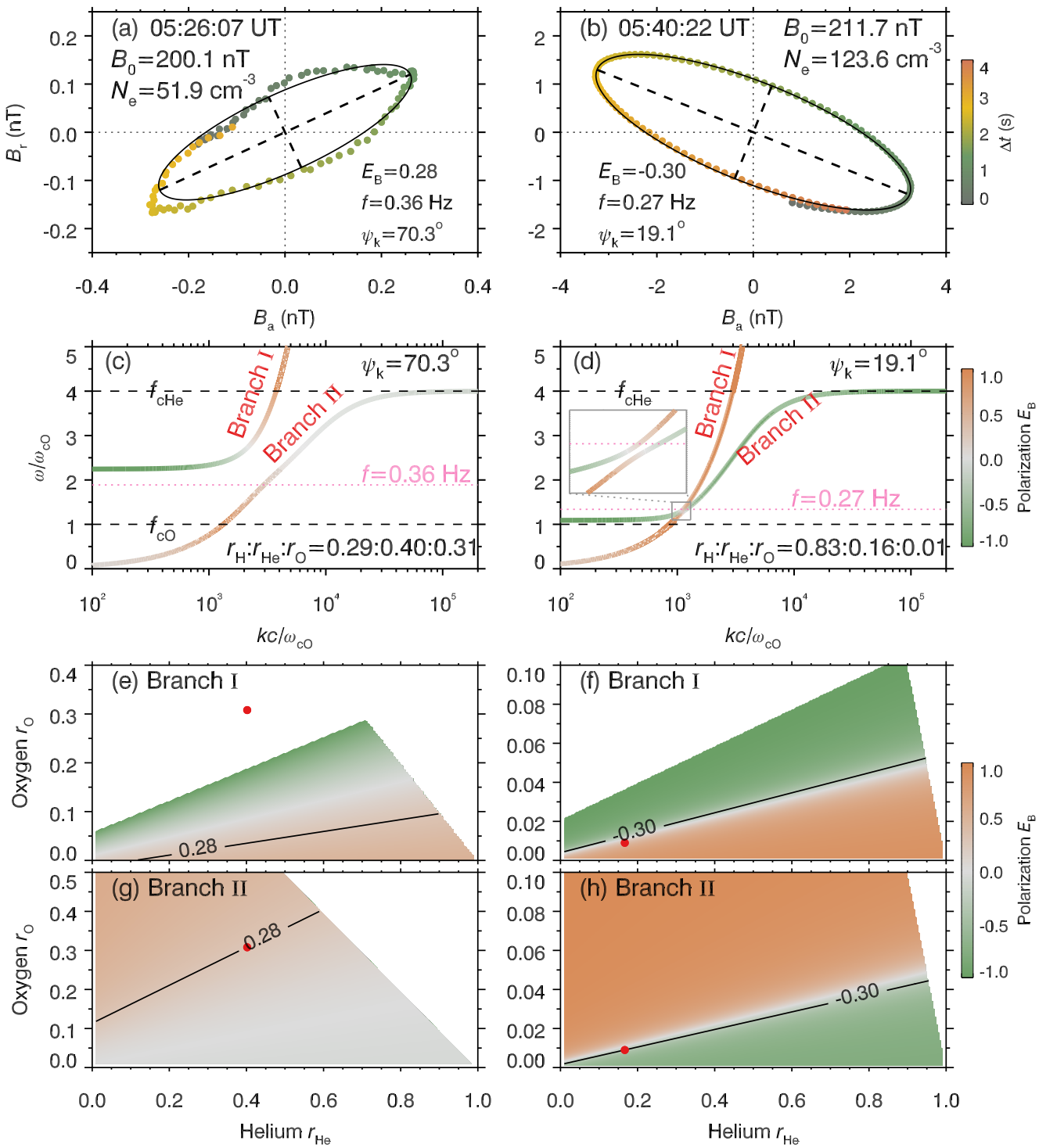

Figure 2. Inference of ion abundances from the polarization of EMIC waves observed at 05:26:07 UT (left column) and 05:40:22 UT (right column). (a and b) $B_a - B_r$ hodograms for EMIC waves. (c and d) EMIC wave dispersion curves color-coded according to polarization values. At each time moment, the selected ion abundances represents one of the possible situations determined through the subsequent analysis of wave polarization and propagation characteristics. Wave polarization values under different ion abundances for (e, f) Branch I and (g, h) Branch II EMIC waves. The red dots mark the selected ion abundances in panels (c, d).

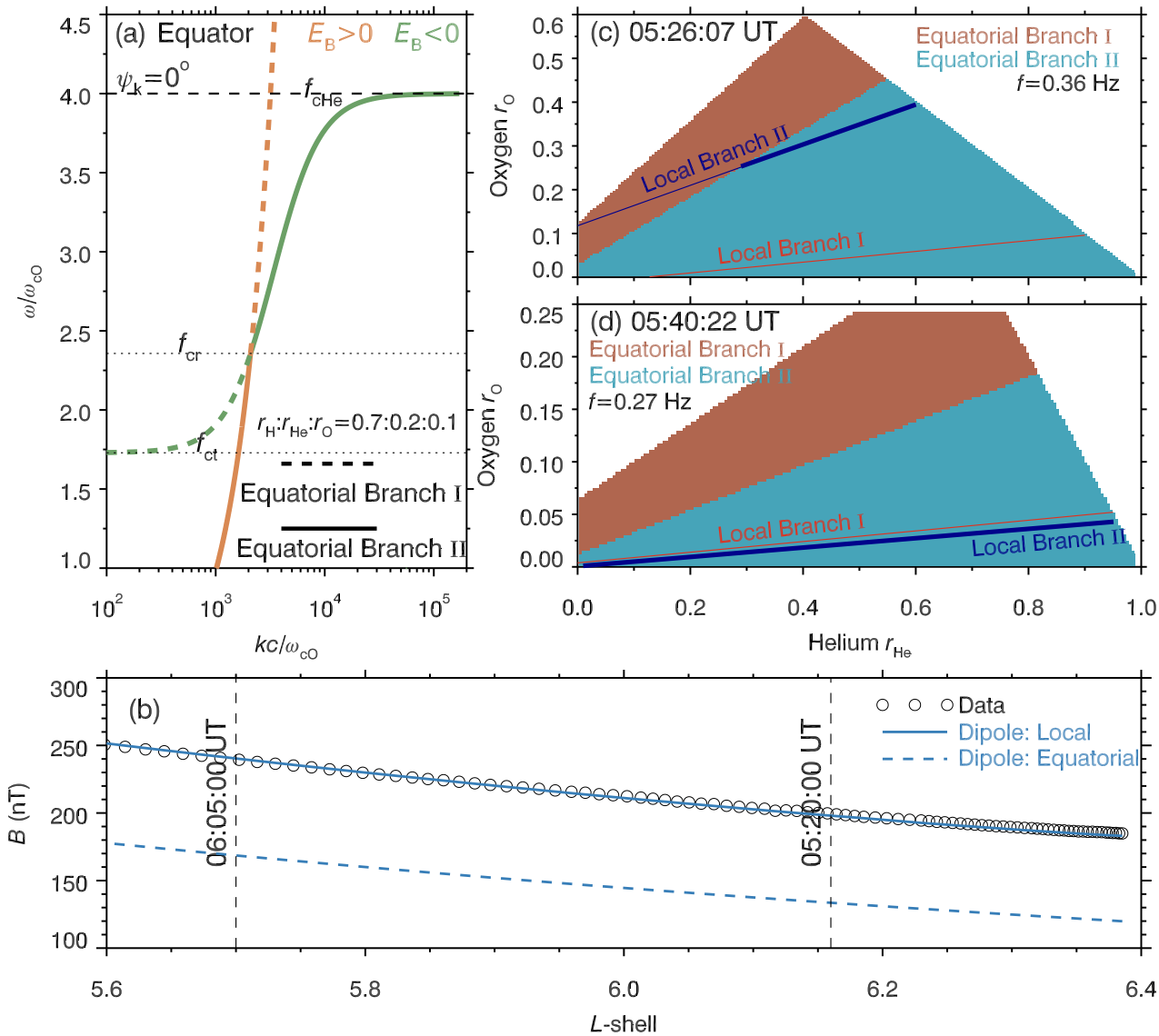

Figure 3. Inference of ion abundances from the propagation characteristics of EMIC waves. (a) Cold plasma dispersion curves for parallel-propagating EMIC waves, with the ion abundance ratio $r_H : r_{He} : r_O = 0.7 : 0.2 : 0.1$ arbitrarily selected to illustrate the results. The green and pumpkin colors help differentiate between the left- and right-handed ploarizations, and the solid and dashed line styles help differentiate between the two dispersion branches at the equator. (b) Local and equatorial background magnetic field. The black circles and blue solid line are observed and dipole-modeled local magnetic fields and the blue dashed line is equatorial magnetic field estimated based on dipole model. (c, d) Overlap of local and equatorial dispersion branches at 05:26:07 UT and 05:40:22 UT. The brown and cyan shadows represent the ion abundances corresponding to equatorial Branch I and II EMIC waves. The overlain red and blue lines represent the allowed ion abundances (Figures 2e–2h) on the local dispersion branches I and II, respectively. The bold portions of these lines represent the matching between the local and equatorial dispersion branches, while the thin portions represent their mismatching.

4. Formation Mechanism of Oxygen Torus

We have totally selected 25 regular wave segments and obtained the corresponding ion abundances using the technique described above (Figures 4a and 4b). Within the plasmaspheric core $L < 6.11$, the inferred O^+ abundance is less than 0.08, and the inferred O^+ density is below 9 cm^{-3}. In the plasmaspheric boundary layer, the inferred O^+ abundance increases steeply from $L = 6.11$ to 6.14 and decreases gradually above $L = 6.14$. The peak O^+ abundance is inferred to be in a range of 0.24–0.40, with the corresponding peak O^+ density in a range of 12–20 cm^{-3}. Although the azimuthal and latitudinal coverages of this O^+ enrichment remain unclear due to the absence of coordinated observations from other satellites, we here still use the traditional term, oxygen torus, to describe this structure. Previous studies have shown that the oxygen torus primarily occurs near the plasmapause

10.1029/2024GL113798

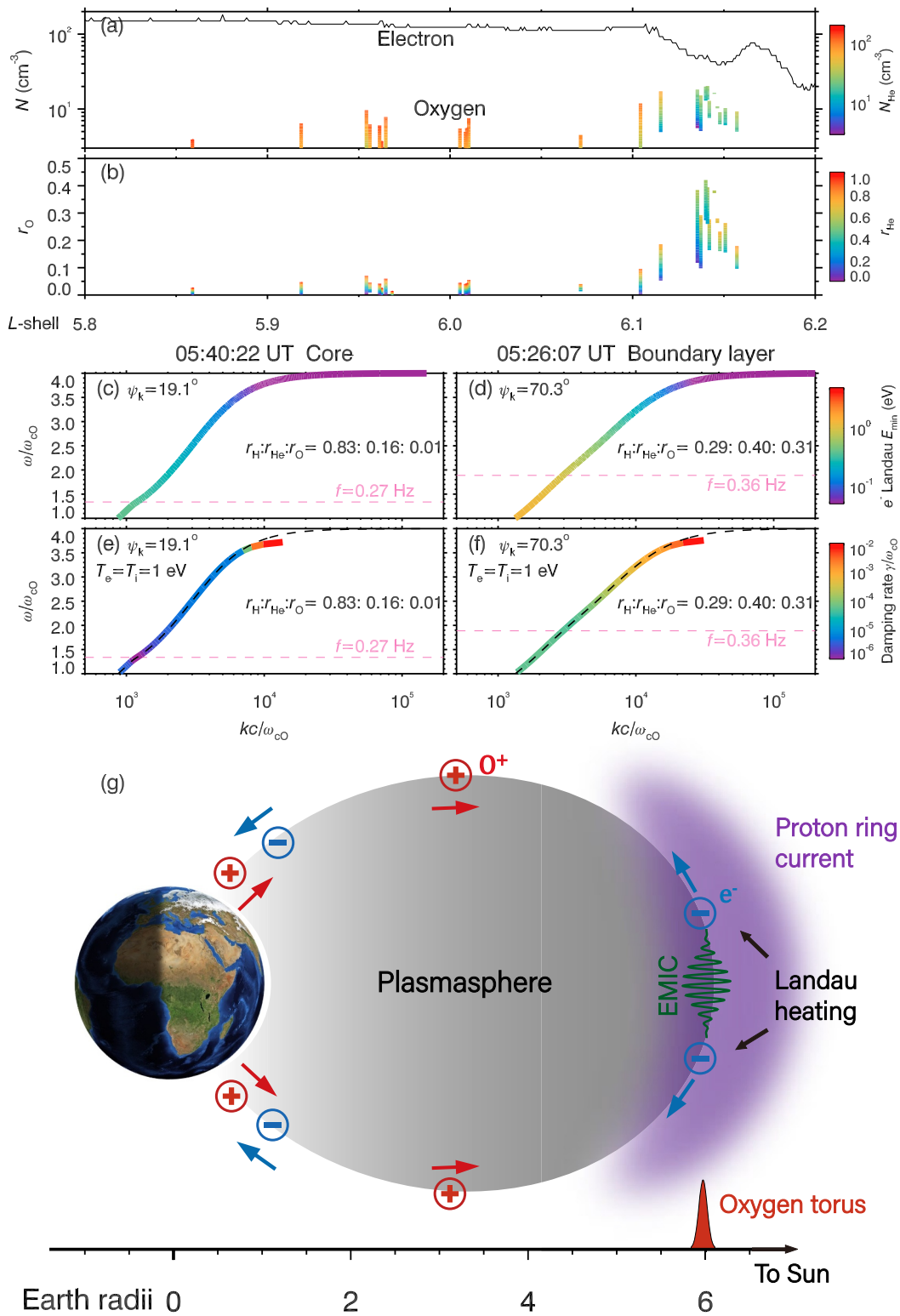

Figure 4. Oxygen torus induced by EMIC waves. Inferred O^+ (a) abundances and (b) densities along the orbit of Van Allen Probe A during 05:24-05:53 UT. The range bars are color-coded according to the He^+ abundance and density. (c, d) Branch II EMIC wave cold plasma dispersion curves color-coded according to minimum Landau resonant energy of electrons E_{min}. (e, f) Branch II EMIC wave hot plasma dispersion curves color-coded according to normalized wave damping rate γ/ω_{cO} with electron and ion temperatures $T_e = T_i = 1$ eV. The overlain dashed lines are cold plasma dispersion curves. (g) Schematic diagram depicting the formation of oxygen torus.

(Chappell, 1982; Gallagher et al., 2016; Goldstein et al., 2018; Horwitz et al., 1984; Nosé et al., 2015, 2018; Roberts et al., 1987) with a center at $L = 3$–5 and a radial width of $\Delta L = 0.5$–1.5. In contrast to most previously investigated events, which were related to geomagnetic storms, the event reported here occurred during quiescent times when the plasmasphere had expanded to $L \approx 6$. The narrowness of the oxygen torus reported here is probably related to the peculiarity in its formation mechanism.

Previous studies have proposed three plausible scenarios for the formation of the oxygen torus: (a) the geomagnetic mass spectrometer effect on the ion outflow from the dayside polar cusp or polar cap region (Roberts et al., 1987); (b) the direct outflow of O^+ ions from the nightside auroral or subauroral regions (Z. Y. Liu & Zong, 2022; Nosé et al., 2022); and (c) the enhanced upwelling of ionospheric O^+ ions in a plasmaspheric background heated by the ring current (Cornwall et al., 1971; Horwitz et al., 1984; Strangeway et al., 2005; Wiltberger, 2015).

In the first two scenarios, the O^+ ion outflow occurs during geomagnetic storms or substorms. For the specific event reported here, we speculate that the dominant O^+ outflow occurred on 9 February 2014, when the SYM-H index reached a minimum of −40 nT and the AE index peaked at 1,200 nT (Figure 1a). Previous numerical calculations have shown that these low-energy (10–10^3 eV) O^+ ions can be transported from the nightside to the dayside within approximately 10 hr (Nosé et al., 2015, 2022). During February 10–13, the plasmasphere was eroded to $L < 4$ multiple times following substorm onsets (Figure 1b). The previously released O^+ ions were unlikely to be still trapped near $L = 6$ but more likely to have escaped through the magnetopause. Therefore, the first two scenarios may not be the primary contributors to the observed oxygen torus in this event.

In the third scenario, the plasmaspheric electrons are envisioned to conduct heat from the ring current to the ionospheric plasma. The underlying mechanisms include the Coulomb collision between ring current protons and plasmaspheric electrons (Cole, 1965; Fok et al., 1991), the Landau heating of plasmaspheric electrons by EMIC waves from the temperature anisotropy instability of ring current protons (Cornwall et al., 1971; Erlandson et al., 1993; Fu et al., 2018; Khazanov et al., 2007; Thorne & Horne, 1992; Thorne et al., 2006; B. Wang et al., 2016; G. Wang et al., 2017; Yuan et al., 2014; Zhou et al., 2013), and the Landau heating of plasmaspheric electrons by hiss waves from the temperature anisotropy instability of ring current electrons (Li et al., 2019; Thorne & Horne, 1994; Z. Wang et al., 2020). Considering the narrow occurrence of oxygen torus in contrast to the large-scale overlap of ring current and plasmasphere and the absence of hiss waves in the density dip (not shown for brevity) where the oxygen torus emerged, we speculate that Coulomb collision and Landau heating by hiss waves are not the primary contributors to the observed oxygen torus in this event. A remained possibility is that the Landau heating by EMIC waves was the primary contributor.

The minimum Landau resonant energy of electrons (Summers et al., 2007) for the observed EMIC waves was on the order of 0.1 eV both in the plasmaspheric core and boundary layer (Figures 4c and 4d). The expected Landau heating of electrons was not observable due to the limited energy coverage of the Helium Oxygen Proton Electron Mass Spectrometer (HOPE) instrument (Funsten et al., 2013) on the Van Allen Probes. In the plasmaspheric core, the EMIC waves were propagating quasi-parallel from the geomagnetic equator to the observer (Figure 1f), probably caused by the density ducting effect (L. Chen et al., 2009; de Soria-Santacruz et al., 2013; Yue et al., 2020). In the density dip of the plasmaspheric boundary layer, where the density gradient approached 0 (Figure 1c), the EMIC wave vectors could have significantly deviated from the parallel direction slight away from the equator (Figure 1f). Figures 4e and 4f show two tests using the Waves in Homogeneous Anisotropic Magnetized Plasma code (Rönnmark, 1982) for waves at the observer with the inferred ion abundances. In these tests, only the thermal electron and ion components with the same temperature of 1 eV are included. The wave Landau damping rate in the plasmaspheric boundary layer is 1–2 orders of magnitude larger than that in the plasmaspheric core, which qualitatively explains the observed difference of wave power between the plasmaspheric core and the plasmaspheric boundary layer at mid-latitudes (Figure 1e). A narrow density dip with obliquely-propagating EMIC waves naturally caused a narrow oxygen torus.

Enhanced heat conduction by hot electrons from the ring current to the ionosphere results in at least two significant outcomes. First, it increases the scale height of ionospheric ions, leading to a closer resemblance between the ion compositions of the ionosphere and the plasmasphere (Roberts et al., 1987). Second, it strengthens the ambipolar electric field, which accelerates oxygen ions to overcome Earth's gravity (Collinson et al., 2024; Ma et al., 2018; Strangeway et al., 2005; Wiltberger, 2015). Given the complexity of these physical processes, a

detailed quantitative analysis is challenging. Therefore, we here qualitatively estimate whether EMIC waves can provide enough energy to facilitate the escape of a sufficient number of oxygen ions into the plasmasphere. As discussed above, the EMIC waves observed inside the density dip had been substantially damped during propagation from the equator to mid-latitudes. Assuming the total Poynting flux of EMIC waves over the entire frequency band at the equator was comparable to that observed inside the plasmaspheric core, approximately $Q \approx 5\ \mu W/m^2$, on the same order as previous measurements (e.g., Loto'Aniu et al., 2005; Ojha et al., 2021). If this wave energy were fully transmitted to ionospheric oxygen ions, we can estimate the required duration for such energy transfer. At $L = 6$, the magnetic flux tube has a length of $H \approx 10\ R_E$ (where $R_E = 6376$ km is Earth's radius). Assuming oxygen ions are uniformly distributed along this tube with a density of $N_O = 10\ cm^{-3}$, and each oxygen ion requires an energy of $E_O \approx 10$ eV to overcome the Earth's gravity, the necessary duration for EMIC waves to provide sufficient energy can be calculated as follows

$$\Delta t = \frac{HN_O E_O}{Q} \approx 200\ \text{s}. \tag{6}$$

This calculation ignores the diverse energy dissipation processes within the atmosphere-ionosphere-plasmasphere coupling system and probably underestimates the actual time required for wave energy input. In the specific event of Figure 1, EMIC waves were continuously observed for about 0.5 hr near the plasmapause. Although the duration before the formation of the oxygen torus was unobservable, it is reasonable to infer that the waves persisted long enough to contribute significantly to the observed oxygen torus formation.

5. Conclusion and Discussion

We have developed a novel approach to infer ion abundances from the polarization and propagation characteristics of EMIC waves within the framework of cold plasma wave theory. In an inner magnetospheric cold plasma containing electrons and three types of singly charged ions, three constraints are required to determine the abundances of these ions. The first constraint ensures the overall charge neutrality in the plasma. The second constraint is derived from the observed instantaneous polarization value of the quasi-monochromatic EMIC wave. The third constraint arises from the invariance of the dispersion branch of the EMIC wave. Specifically, the EMIC wave is initially generated as a left-handed polarized wave with a wave vector parallel to the magnetic field at the geomagnetic equator. As the wave propagates away from the equator, its wave vector gradually becomes oblique but it persists on the same dispersion branch.

By applying this approach, we have identified a narrow oxygen torus in the noonside plasmaspheric boundary layer during a quiet period. This oxygen torus centered around $L \approx 6.14$, with a radial width of $\Delta L = 0.05$. At the center of this oxygen torus, the O^+ abundance ranged from 0.24 to 0.40, and the O^+ density ranged from 12 to 20 cm^{-3}. The large radial distance of this oxygen torus from Earth was related to the expansion of the plasmasphere during the quiet period. The radial narrowness of the oxygen torus was associated with the spatial structure of the plasmaspheric boundary layer. A plausible scenario for the formation of this oxygen torus is as follows (Figure 4g): (a) the ring current protons excited EMIC waves through a combination of linear and nonlinear processes in the outer plasmasphere at the equator; (b) within the density dip embedded in the plasmaspheric boundary layer, the EMIC waves propagated away from the equator with their wave vectors gradually becoming oblique relative to the background magnetic field; (c) the obliquely propagating EMIC waves can cause parallel heating of cold plasmaspheric electrons, which eventually conducted heat to the ionospheric plasma and promoted the upwelling of ionospheric O^+ ions into the magnetosphere. However, due to the limitations in instrumental capability and space mission coverage, the Landau heating of cold plasmaspheric electrons and the upwelling of oxygen ions were not directly identified. While the exact mechanisms remain complex, qualitative estimates suggest that EMIC waves could supply sufficient energy over extended periods to promote the escape of oxygen ions into the plasmasphere.

Compared to the oxygen torus described by Roberts et al. (1987), EMIC waves exhibit a significantly lower occurrence probability (Meredith et al., 2014; Min et al., 2012; Usanova et al., 2012; Zhang et al., 2016). Two main possibilities can explain this discrepancy (Horwitz et al., 1984; Roberts et al., 1987; Usanova, 2021; Zhang et al., 2016). First, the lifetimes of EMIC waves and the oxygen torus differ. EMIC waves may arise within a relatively short time period but still inject substantial energy into the ionosphere. In contrast, cold oxygen ions

require 1–2 hr to transport from the ionosphere to the plasmasphere and remain there for extended periods until the next plasmaspheric reformation. Second, beyond the EMIC-related scenario proposed here, other mechanisms must also play a role in the formation of the oxygen torus (Cornwall et al., 1971; Horwitz et al., 1984; Z. Y. Liu & Zong, 2022; Nosé et al., 2022; Roberts et al., 1987; Strangeway et al., 2005; Wiltberger, 2015). Future research should focus on validating this EMIC wave-related hypothesis for the formation of the oxygen torus and evaluating its relative importance compared to alternative processes. This will require the development and utilization of advanced satellite missions and instruments to provide more comprehensive and detailed observations. Collaborative efforts across multiple satellite projects will be essential to achieve a deeper understanding of the processes involved in the formation and evolution of the oxygen torus within the magnetosphere-ionosphere coupling system.

Data Availability Statement

Van Allen Probes data are available at https://spdf.gsfc.nasa.gov/pub/data/rbsp/; SYM-H (World Data Center for Geomagnetism, Kyoto et al., 2022) and AE (World Data Center for Geomagnetism, Kyoto et al., 2015) data are available at https://wdc.kugi.kyoto-u.ac.jp/wdc/Sec3.html. In this work, we have analyzed the following data: EMFISIS L2 WFR Cross Spectral Matrix data at https://cdaweb.gsfc.nasa.gov/; L3 MAG magnetic field data (Kletzing, 2022); L4 HFR density data (Kurth et al., 2022); L2 EFW electric field data (Wygant, 2022); ECT L3 HOPE Plasma Moments data (Funsten et al., 2022). WHAMP code is available at https://github.com/irfu/whamp/.

Acknowledgments
We acknowledge EMFISIS, EFW and ECT teams for the use of Van Allen Probes data and WDC for Geomagnetism (Kyoto) for providing the SYM-H and AE indices. We thank Masahito Nosé for his insightful suggestions on this study. This work was supported by the National Natural Science Foundation of China Grants 42188101, 42130204, 42441808 and 42274198, the Postdoctoral Fellowship Program of China Postdoctoral Science Foundation GZB20240701, and the open project fund of State Key Laboratory of Lunar and Planetary Sciences (Macau University of Science and Technology) (Macau FDCT Grant 002/2024/SKL).

References

An, Z., Tao, X., Zonca, F., & Chen, L. (2024). Frequency chirping of electromagnetic ion cyclotron waves in Earth's magnetosphere. *Geophysical Research Letters*, *51*(4), e2023GL106456. https://doi.org/10.1029/2023GL106456

Cao, X., Ni, B., Summers, D., Ma, X., Lou, Y., Zhang, Y., et al. (2020). Effects of superthermal plasmas on the linear growth of multiband EMIC waves. *The Astrophysical Journal*, *899*(1), 43. https://doi.org/10.3847/1538-4357/ab9ec4

Capannolo, L., Li, W., Ma, Q., Chen, L., Shen, X. C., Spence, H. E., et al. (2019). Direct observation of subrelativistic electron precipitation potentially driven by EMIC waves. *Geophysical Research Letters*, *46*(22), 12711–12721. https://doi.org/10.1029/2019GL084202

Chappell, C. R. (1982). Initial observations of thermal plasma composition and energetics from Dynamics Explorer-1. *Geophysical Research Letters*, *9*(9), 929–932. https://doi.org/10.1029/GL009i009p00929

Chappell, C. R., Fields, S. A., Baugher, C. R., Hoffman, J. H., Hanson, W. B., Wright, W. W., et al. (1981). The retarding ion mass spectrometer on Dynamics Explorer-A. *Space Science Instrumentation*, *5*, 477–491.

Chen, H., Gao, X., Lu, Q., Tsurutani, B. T., & Wang, S. (2020). Statistical evidence for EMIC wave excitation driven by substorm injection and enhanced solar wind pressure in the Earth's magnetosphere: Two different EMIC wave sources. *Geophysical Research Letters*, *47*(21), e90275. https://doi.org/10.1029/2020GL090275

Chen, L., Thorne, R. M., & Horne, R. B. (2009). Simulation of EMIC wave excitation in a model magnetosphere including structured high-density plumes. *Journal of Geophysical Research*, *114*(A7), A07221. https://doi.org/10.1029/2009JA014204

Chen, L., Thorne, R. M., Shprits, Y., & Ni, B. (2013). An improved dispersion relation for parallel propagating electromagnetic waves in warm plasmas: Application to electron scattering. *Journal of Geophysical Research: Space Physics*, *118*(5), 2185–2195. https://doi.org/10.1002/jgra.50260

Chen, Z., Tian, H., Li, H., Tang, R., Ouyang, Z., & Deng, X. (2023). The study on the global evolution of energetic electron precipitation during geomagnetic storm based on deep learning algorithm. *Journal of Geophysical Research: Space Physics*, *128*(3), e2022JA030974. https://doi.org/10.1029/2022JA030974

Cole, K. D. (1965). Stable auroral red arcs, sinks for energy of D_{st} main phase. *Journal of Geophysical Research*, *70*(7), 1689–1706. https://doi.org/10.1029/JZ070i007p01689

Collinson, G. A., Glocer, A., Pfaff, R., Barjatya, A., Conway, R., Breneman, A., et al. (2024). Earth's ambipolar electrostatic field and its role in ion escape to space. *Nature*, *632*(8027), 1021–1025. https://doi.org/10.1038/s41586-024-07480-3

Cornwall, J. M., Coroniti, F. V., & Thorne, R. M. (1971). Unified theory of SAR arc formation at the plasmapause. *Journal of Geophysical Research*, *76*(19), 4428–4445. https://doi.org/10.1029/JA076i019p04428

de Soria-Santacruz, M., Spasojevic, M., & Chen, L. (2013). EMIC waves growth and guiding in the presence of cold plasma density irregularities. *Geophysical Research Letters*, *40*(10), 1940–1944. https://doi.org/10.1002/grl.50484

Erlandson, R. E., Aggson, T. L., Hogey, W. R., & Slavin, J. A. (1993). Simultaneous observations of subauroral electron temperature enhancements and electromagnetic ion cyclotron waves. *Geophysical Research Letters*, *20*(16), 1723–1726. https://doi.org/10.1029/93GL01975

Fok, M. C., Kozyra, J. U., Nagy, A. F., & Cravens, T. E. (1991). Lifetime of ring current particles due to Coulomb collisions in the plasmasphere. *Journal of Geophysical Research*, *96*(A5), 7861–7868. https://doi.org/10.1029/90JA02620

Fraser, B. J., Horwitz, J. L., Slavin, J. A., Dent, Z. C., & Mann, I. R. (2005). Heavy ion mass loading of the geomagnetic field near the plasmapause and ULF wave implications. *Geophysical Research Letters*, *32*(4), L04102. https://doi.org/10.1029/2004GL021315

Fraser, B. J., Singer, H. J., Hughes, W. J., Wygant, J. R., Anderson, R. R., & Hu, Y. D. (1996). CRRES poynting vector observations of electromagnetic ion cyclotron waves near the plasmapause. *Journal of Geophysical Research*, *101*(A7), 15331–15344. https://doi.org/10.1029/95JA03480

Fu, S., Ni, B., Lou, Y., Bortnik, J., Ge, Y., Tao, X., et al. (2018). Resonant scattering of near-equatorially mirroring electrons by Landau resonance with H^+ band EMIC waves. *Geophysical Research Letters*, *45*(20), 10866–10873. https://doi.org/10.1029/2018GL079718

Funsten, H. O., Skoug, R. M., Guthrie, A. A., MacDonald, E. A., Baldonado, J. R., Harper, R. W., et al. (2013). Helium, oxygen, proton, and electron (HOPE) mass spectrometer for the radiation belt storm Probes mission. *Space Science Reviews*, *179*(1–4), 423–484. https://doi.org/10.1007/s11214-013-9968-7

Funsten, H. O., Skoug, R. M., Larsen, B. A., & Friedel, R. (2022). Van allen Probe A energetic particle, composition, and thermal plasma suite (ECT) helium oxygen proton electron electrostatic analyzer (HOPE) spin-resolved science data. Electron >200 eV and ion >30 eV plasma moments measured at apogee in alternate spin cadence, level 3, release 4 (L3), 24.35 s data [Dataset]. *NASA Space Physics Data Facility*. https://doi.org/10.48322/egeg-7005

Gallagher, D. L., Goldstein, J., Craven, P. D., & Comfort, R. H. (2016). Revisiting the inner magnetospheric oxygen torus with DE 1 RIMS. In *Agu fall meeting abstracts* (pp. SM33C–2521).

Geiss, J., & Young, D. T. (1981). Production and transport of O^{++} in the ionosphere and plasmasphere. *Journal of Geophysical Research*, *86*(A6), 4739–4750. https://doi.org/10.1029/JA086iA06p04739

Goldstein, J., Chappell, C. R., Davis, M. W., Denton, M. H., Denton, R. E., Gallagher, D. L., et al. (2018). Imaging the global distribution of plasmaspheric oxygen. *Journal of Geophysical Research (Space Physics)*, *123*(3), 2078–2103. https://doi.org/10.1002/2017JA024531

Henning, F. D., & Mace, R. L. (2014). Effects of ion abundances on electromagnetic ion cyclotron wave growth rate in the vicinity of the plasmapause. *Physics of Plasmas*, *21*(4), 042905. https://doi.org/10.1063/1.4873375

Horne, R. B., & Miyoshi, Y. (2016). Propagation and linear mode conversion of magnetosonic and electromagnetic ion cyclotron waves in the radiation belts. *Geophysical Research Letters*, *43*(19), 10. https://doi.org/10.1002/2016GL070216

Horne, R. B., & Thorne, R. M. (1990). Ion cyclotron absorption at the second harmonic of the oxygen gyrofrequency. *Geophysical Research Letters*, *17*(12), 2225–2228. https://doi.org/10.1029/GL017i012p02225

Horne, R. B., & Thorne, R. M. (1993). On the preferred source location for the convective amplification of ion cyclotron waves. *Journal of Geophysical Research*, *98*(A6), 9233–9247. https://doi.org/10.1029/92JA02972

Horwitz, J. L., Comfort, R. H., & Chappell, C. R. (1984). Thermal ion composition measurements of the formation of the new outer plasmasphere and double plasmapause during storm recovery phase. *Geophysical Research Letters*, *11*(8), 701–704. https://doi.org/10.1029/GL011i008p00701

Hull, A. J., Chaston, C. C., Bonnell, J. W., Wygant, J. R., Kletzing, C. A., Reeves, G. D., & Gerrard, A. (2019). Dispersive Alfvén wave control of O^+ ion outflow and energy densities in the inner magnetosphere. *Geophysical Research Letters*, *46*(15), 8597–8606. https://doi.org/10.1029/2019GL083808

Jordanova, V. K., Albert, J., & Miyoshi, Y. (2008). Relativistic electron precipitation by EMIC waves from self-consistent global simulations. *Journal of Geophysical Research*, *113*(A3), A00A10. https://doi.org/10.1029/2008JA013239

Keika, K., Kistler, L. M., & Brandt, P. C. (2013). Energization of O^+ ions in the Earth's inner magnetosphere and the effects on ring current buildup: A review of previous observations and possible mechanisms. *Journal of Geophysical Research: Space Physics*, *118*(7), 4441–4464. https://doi.org/10.1002/jgra.50371

Khazanov, G. V., Gamayunov, K. V., Gallagher, D. L., Kozyra, J. U., & Liemohn, M. W. (2007). Self-consistent model of magnetospheric ring current and propagating electromagnetic ion cyclotron waves: 2. Wave-Induced ring current precipitation and thermal electron heating. *Journal of Geophysical Research*, *112*(A4), A04209. https://doi.org/10.1029/2006JA012033

Kletzing, C. A. (2022). Van allen Probe A fluxgate magnetometer high resolution data in GSM coordinates [Dataset]. *NASA Space Physics Data Facility*. https://doi.org/10.48322/2tyy-s986

Kletzing, C. A., Kurth, W. S., Acuna, M., MacDowall, R. J., Torbert, R. B., Averkamp, T., et al. (2013). The electric and magnetic field instrument suite and integrated science (EMFISIS) on RBSP. *Space Science Reviews*, *179*(1–4), 127–181. https://doi.org/10.1007/s11214-013-9993-6

Kronberg, E. A., Ashour-Abdalla, M., Dandouras, I., Delcourt, D. C., Grigorenko, E. E., Kistler, L. M., et al. (2014). Circulation of heavy ions and their dynamical effects in the magnetosphere: Recent observations and models. *Space Science Reviews*, *184*(1–4), 173–235. https://doi.org/10.1007/s11214-014-0104-0

Kurth, W. S., De Pascuale, S., Faden, J. B., Kletzing, C. A., Hospodarsky, G. B., Thaller, S., & Wygant, J. R. (2015). Electron densities inferred from plasma wave spectra obtained by the Waves instrument on Van Allen Probes. *Journal of Geophysical Research: Space Physics*, *120*(2), 904–914. https://doi.org/10.1002/2014JA020857

Kurth, W. S., De Pascuale, S., Faden, J. B., Kletzing, C. A., Hospodarsky, G. B., Thaller, S. A., & Wygant, J. R. (2022). Van allen Probe A electric and magnetic field instrument suite and integrated science (EMFISIS) density and other parameters derived by digitizing traces on spectrograms, level 4 (L4), 0.5 s data [Dataset]. *NASA Space Physics Data Facility*. https://doi.org/10.48322/c4ha-xj50

Lemaire, J. F., & Gringauz, K. I. (1998). *The Earth's plasmasphere*. Cambridge University Press.

Li, J., Ma, Q., Bortnik, J., Li, W., An, X., Reeves, G. D., et al. (2019). Parallel acceleration of suprathermal electrons caused by whistler-mode hiss waves. *Geophysical Research Letters*, *46*(22), 12675–12684. https://doi.org/10.1029/2019GL085562

Liu, N., Su, Z., Gao, Z., Zheng, H., Wang, Y., & Wang, S. (2020). Can solar wind decompressive discontinuities suppress magnetospheric electromagnetic ion cyclotron waves associated with fresh proton injections? *Geophysical Research Letters*, *47*(17), e90296. https://doi.org/10.1029/2020GL090296

Liu, S., Xia, Z., Chen, L., Liu, Y., Liao, Z., & Zhu, H. (2019). Magnetospheric multiscale observation of quasiperiodic EMIC waves associated with enhanced solar wind pressure. *Geophysical Research Letters*, *46*(13), 7096–7104. https://doi.org/10.1029/2019GL083421

Liu, Z. Y., & Zong, Q. G. (2022). Ionospheric oxygen outflows directly injected into the inner magnetosphere: Van allen Probes statistics. *Journal of Geophysical Research (Space Physics)*, *127*(10), e2022JA030611. https://doi.org/10.1029/2022JA030611

Loto'Aniu, T. M., Fraser, B. J., & Waters, C. L. (2005). Propagation of electromagnetic ion cyclotron wave energy in the magnetosphere. *Journal of Geophysical Research*, *110*(A7), A07214. https://doi.org/10.1029/2004JA010816

Ma, Y.-Z., Zhang, Q.-H., Xing, Z.-Y., Heelis, R. A., Oksavik, K., & Wang, Y. (2018). The ion/electron temperature characteristics of polar cap classical and hot patches and their influence on ion upflow. *Geophysical Research Letters*, *45*(16), 8072–8080. https://doi.org/10.1029/2018GL079099

Mauk, B. H., Fox, N. J., Kanekal, S. G., Kessel, R. L., Sibeck, D. G., & Ukhorskiy, A. (2013). Science objectives and rationale for the radiation belt storm Probes mission. *Space Science Reviews*, *179*(1–4), 3–27. https://doi.org/10.1007/s11214-012-9908-y

McCollough, J. P., Elkington, S. R., & Baker, D. N. (2009). Modeling EMIC wave growth during the compression event of 29 June 2007. *Geophysical Research Letters*, *36*(18), L18108. https://doi.org/10.1029/2009GL039985

Meredith, N. P., Horne, R. B., Kersten, T., Fraser, B. J., & Grew, R. S. (2014). Global morphology and spectral properties of EMIC waves derived from CRRES observations. *Journal of Geophysical Research: Space Physics*, *119*(7), 5328–5342. https://doi.org/10.1002/2014JA020064

Min, K., Lee, J., Keika, K., & Li, W. (2012). Global distribution of EMIC waves derived from THEMIS observations. *Journal of Geophysical Research*, *117*(A5), A05219. https://doi.org/10.1029/2012JA017515

Miyoshi, Y., Matsuda, S., Kurita, S., Nomura, K., Keika, K., Shoji, M., et al. (2019). EMIC waves converted from equatorial noise due to M/Q = 2 ions in the plasmasphere: Observations from Van Allen Probes and arase. *Geophysical Research Letters*, *46*(11), 5662–5669. https://doi.org/10.1029/2019GL083024

Miyoshi, Y., Sakaguchi, K., Shiokawa, K., Evans, D., Albert, J., Connors, M., & Jordanova, V. (2008). Precipitation of radiation belt electrons by EMIC waves, observed from ground and space. *Geophysical Research Letters*, *35*(23), L23101. https://doi.org/10.1029/2008GL035727

Morley, S. K., Ables, S. T., Sciffer, M. D., & Fraser, B. J. (2009). Multipoint observations of Pc1-2 waves in the afternoon sector. *Journal of Geophysical Research*, *114*(A9), 9205. https://doi.org/10.1029/2009JA014162

Nosé, M., Matsuoka, A., Kumamoto, A., Kasahara, Y., Goldstein, J., Teramoto, M., et al. (2018). Longitudinal structure of oxygen torus in the inner magnetosphere: Simultaneous observations by arase and van Allen Probe A. *Geophysical Research Letters*, *45*(19), 10177–10184. https://doi.org/10.1029/2018GL080122

Nosé, M., Matsuoka, A., Kumamoto, A., Kasahara, Y., Teramoto, M., Kurita, S., et al. (2020). Oxygen torus and its coincidence with EMIC wave in the deep inner magnetosphere: Van Allen Probe B and Arase observations. *Earth Planets and Space*, *72*(1), 111. https://doi.org/10.1186/s40623-020-01235-w

Nosé, M., Matsuoka, A., Miyoshi, Y., Asamura, K., Hori, T., Teramoto, M., et al. (2022). Flux enhancements of field-aligned low-energy O^+ ion (FALEO) in the inner magnetosphere: A possible source of warm plasma cloak and oxygen torus. *Journal of Geophysical Research (Space Physics)*, *127*(3), e30008. https://doi.org/10.1029/2021JA030008

Nosé, M., Oimatsu, S., Keika, K., Kletzing, C. A., Kurth, W. S., de Pascuale, S., et al. (2015). Formation of the oxygen torus in the inner magnetosphere: Van Allen Probes observations. *Journal of Geophysical Research: Space Physics*, *120*(2), 1182–1196. https://doi.org/10.1002/2014JA020593

Ojha, B., Omura, Y., Singh, S., & Lakhina, G. S. (2021). Multipoint analysis of source regions of EMIC waves and rapid growth of subpackets. *Journal of Geophysical Research: Space Physics*, *126*(11), e29514. https://doi.org/10.1029/2021JA029514

Omidi, N., Bortnik, J., Thorne, R., & Chen, L. (2013). Impact of cold O^+ ions on the generation and evolution of EMIC waves. *Journal of Geophysical Research: Space Physics*, *118*(1), 434–445. https://doi.org/10.1029/2012JA018319

Omura, Y., Pickett, J., Grison, B., Santolik, O., Dandouras, I., Engebretson, M., et al. (2010). Theory and observation of electromagnetic ion cyclotron triggered emissions in the magnetosphere. *Journal of Geophysical Research*, *115*(A7), 7234. https://doi.org/10.1029/2010JA015300

Pickett, J. S., Grison, B., Omura, Y., Engebretson, M. J., Dandouras, I., Masson, A., et al. (2010). Cluster observations of EMIC triggered emissions in association with Pc1 waves near Earth's plasmapause. *Geophysical Research Letters*, *37*(9), 9104. https://doi.org/10.1029/2010GL042648

Press, W. H. (2007). Numerical recipes. In *The art of scientific computing* (3rd ed.). Cambridge University Press.

Rauch, J. L., & Roux, A. (1982). Ray tracing of ULF waves in a multicomponent magnetospheric plasma: Consequences for the generation mechanism of ion cyclotron waves. *Journal of Geophysical Research*, *87*(A10), 8191–8198. https://doi.org/10.1029/JA087iA10p08191

Roberts, W. T., Jr., Horwitz, J. L., Comfort, R. H., Chappell, C. R., Waite, J. H., & Green, J. L. (1987). Heavy ion density enhancements in the outer plasmasphere. *Journal of Geophysical Research*, *92*(A12), 13499–13512. https://doi.org/10.1029/JA092iA12p13499

Rönnmark, K. (1982). Waves in homogeneous, anisotropic, multicomponent plasmas. Kiruna Geophys. Inst. Rep, 179 (p. 55).

Santolík, O., Parrot, M., & Lefeuvre, F. (2003). Singular value decomposition methods for wave propagation analysis. *Radio Science*, *38*(1), 1010. https://doi.org/10.1029/2000RS002523

Santolík, O., Pickett, J. S., Gurnett, D. A., Menietti, J. D., Tsurutani, B. T., & Verkhoglyadova, O. (2010). Survey of Poynting flux of whistler mode chorus in the outer zone. *Journal of Geophysical Research*, *115*(A7), A00F13. https://doi.org/10.1029/2009JA014925

Santolík, O., Pickett, J. S., Gurnett, D. A., & Storey, L. R. O. (2002). Magnetic component of narrowband ion cyclotron waves in the auroral zone. *Journal of Geophysical Research*, *107*(A12), 1444. https://doi.org/10.1029/2001JA000146

Shay, M. A., & Swisdak, M. (2004). Three-species collisionless reconnection: Effect of O^+ on magnetotail reconnection. *Physical Review Letters*, *93*(17), 175001. https://doi.org/10.1103/PhysRevLett.93.175001

Shoji, M., & Omura, Y. (2011). Simulation of electromagnetic ion cyclotron triggered emissions in the Earth's inner magnetosphere. *Journal of Geophysical Research*, *116*(A5), A05212. https://doi.org/10.1029/2010JA016351

Sonnerup, B. U. O., & Cahill, L. J., Jr. (1967). Magnetopause structure and attitude from explorer 12 observations. *Journal of Geophysical Research*, *72*(1), 171. https://doi.org/10.1029/JZ072i001p00171

Stix, T. H. (1962). *The theory of plasma waves*. McGraw-Hill.

Strangeway, R. J., Ergun, R. E., Su, Y. J., Carlson, C. W., & Elphic, R. C. (2005). Factors controlling ionospheric outflows as observed at intermediate altitudes. *Journal of Geophysical Research*, *110*(A3), A03221. https://doi.org/10.1029/2004JA010829

Su, Z., Zhu, H., Xiao, F., Zheng, H., Zhang, M., Liu, Y. C.-M., et al. (2014). Latitudinal dependence of nonlinear interaction between electromagnetic ion cyclotron wave and terrestrial ring current ions. *Physics of Plasmas*, *21*(5), 052310. https://doi.org/10.1063/1.4880036

Summers, D., Ni, B., & Meredith, N. P. (2007). Timescales for radiation belt electron acceleration and loss due to resonant wave-particle interactions: 1. Theory. *Journal of Geophysical Research*, *112*(A4), A04206. https://doi.org/10.1029/2006JA011801

Takahashi, K., Denton, R. E., Anderson, R. R., & Hughes, W. J. (2006). Mass density inferred from toroidal wave frequencies and its comparison to electron density. *Journal of Geophysical Research*, *111*(A1), A01201. https://doi.org/10.1029/2005JA011286

Takahashi, K., Hartinger, M. D., Angelopoulos, V., & Glassmeier, K.-H. (2015). A statistical study of fundamental toroidal mode standing Alfvén waves using THEMIS ion bulk velocity data. *Journal of Geophysical Research: Space Physics*, *120*(8), 6474–6495. https://doi.org/10.1002/2015JA021207

Tao, X., & Bortnik, J. (2010). Nonlinear interactions between relativistic radiation belt electrons and oblique whistler mode waves. *Nonlinear Processes in Geophysics*, *17*(5), 599–604. https://doi.org/10.5194/npg-17-599-2010

Teng, S., Liu, N., Ma, Q., Tao, X., & Li, W. (2021). Direct observational evidence of the simultaneous excitation of electromagnetic ion cyclotron waves and magnetosonic waves by an anisotropic proton ring distribution. *Geophysical Research Letters*, *48*(8), e91850. https://doi.org/10.1029/2020GL091850

Thorne, R. M., & Horne, R. B. (1992). The contribution of ion-cyclotron waves to electron heating and SAR-arc excitation near the storm-time plasmapause. *Geophysical Research Letters*, *19*(4), 417–420. https://doi.org/10.1029/92GL00089

Thorne, R. M., & Horne, R. B. (1994). Landau damping of magnetospherically reflected whistlers. *Journal of Geophysical Research*, *99*(A9), 17249–17258. https://doi.org/10.1029/94JA01006

Thorne, R. M., Horne, R. B., Jordanova, V. K., Bortnik, J., & Glauert, S. (2006). Interaction of EMIC waves with thermal plasma and radiation belt particles. In K. Takahashi, P. J. Chi, R. E. Denton, & R. L. Lysak (Eds.), *Magnetospheric ULF waves: Synthesis and new directions* (Vol. 169, pp. 213–223). https://doi.org/10.1029/169GM14

Usanova, M. E. (2021). Energy exchange between electromagnetic ion cyclotron (EMIC) waves and thermal plasma: From theory to observations. *Frontiers in Astronomy and Space Sciences*, *8*, 150. https://doi.org/10.3389/fspas.2021.744344

Usanova, M. E., Mann, I. R., Bortnik, J., Shao, L., & Angelopoulos, V. (2012). THEMIS observations of electromagnetic ion cyclotron wave occurrence: Dependence on AE, SYMH, and solar wind dynamic pressure. *Journal of Geophysical Research*, *117*(A10), A10218. https://doi.org/10.1029/2012JA018049

Wang, B., Su, Z., Zhang, Y., Shi, S., & Wang, G. (2016). Nonlinear Landau resonant scattering of near equatorially mirroring radiation belt electrons by oblique EMIC waves. *Geophysical Research Letters*, *43*(8), 3628–3636. https://doi.org/10.1002/2016GL068467

Wang, G., Su, Z., Zheng, H., Wang, Y., Zhang, M., & Wang, S. (2017). Nonlinear fundamental and harmonic cyclotron resonant scattering of radiation belt ultrarelativistic electrons by oblique monochromatic EMIC waves. *Journal of Geophysical Research: Space Physics*, *122*(2), 1928–1945. https://doi.org/10.1002/2016JA023451

Wang, Z., Su, Z., Liu, N., Dai, G., Zheng, H., Wang, Y., & Wang, S. (2020). Suprathermal electron evolution under the competition between plasmaspheric plume hiss wave heating and collisional cooling. *Geophysical Research Letters*, *47*(19), e89649. https://doi.org/10.1029/2020GL089649

Wiltberger, M. (2015). Review of global simulation studies of effect of ionospheric outflow on magnetosphere-ionosphere system dynamics. In A. Keiling, C. M. Jackman, & P. A. Delamere (Eds.), *Magnetotails in the solar system* (Vol. 207, pp. 373–392). https://doi.org/10.1002/9781118842324.ch22

World Data Center for Geomagnetism, Kyoto, Nose, M., Iyemori, T., Sugiura, M., & Kamei, T. (2015). Geomagnetic AE index [Dataset]. *World Data Center for Geomagnetism*. https://doi.org/10.17593/15031-54800

World Data Center for Geomagnetism, Kyoto, Imajo, S., Matsuoka, A., Toh, H., & Iyemori, T. (2022). Mid-latitude geomagnetic indices ASY and SYM (ASY/SYM indices) [Dataset]. *World Data Center for Geomagnetism, Kyoto*. https://doi.org/10.14989/267216

Wygant, J. R. (2022). Van Allen Probe A Electric Fields and Waves (EFW) 32 sample/sec despun electric field in modified-GSE (MGSE) coordinates [Dataset]. *NASA Space Physics Data Facility*. https://doi.org/10.48322/t40m-em97

Wygant, J. R., Bonnell, J. W., Goetz, K., Ergun, R. E., Mozer, F. S., Bale, S. D., et al. (2013). The electric field and waves instruments on the radiation belt storm Probes mission. *Space Science Reviews*, *179*(1–4), 183–220. https://doi.org/10.1007/s11214-013-0013-7

Xiao, F., Zhou, Q., He, H., Zheng, H., & Wang, S. (2007). Electromagnetic ion cyclotron waves instability threshold condition of suprathermal protons by kappa distribution. *Journal of Geophysical Research*, *112*(A7), A07219. https://doi.org/10.1029/2006JA012050

Yau, A. W., & André, M. (1997). Sources of ion outflow in the high latitude ionosphere. *Space Science Reviews*, *80*(1/2), 1–25. https://doi.org/10.1023/A:1004947203046

Yau, A. W., Howarth, A., Peterson, W. K., & Abe, T. (2012). Transport of thermal-energy ionospheric oxygen (O^+) ions between the ionosphere and the plasma sheet and ring current at quiet times preceding magnetic storms. *Journal of Geophysical Research*, *117*(A7), A07215. https://doi.org/10.1029/2012JA017803

Yau, A. W., Shelley, E. G., Peterson, W. K., & Lenchyshyn, L. (1985). Energetic auroral and polar ion outflow at DE 1 altitudes: Magnitude, composition, magnetic activity dependence, and long-term variations. *Journal of Geophysical Research*, *90*(A9), 8417–8432. https://doi.org/10.1029/JA090iA09p08417

Yin, Z.-F., Zhou, X.-Z., Hu, Z.-J., Yue, C., Zong, Q.-G., Hao, Y.-X., et al. (2022). Localized excitation of electromagnetic ion cyclotron waves from anisotropic protons filtered by magnetic dips. *Journal of Geophysical Research: Space Physics*, *127*(6), e30531. https://doi.org/10.1029/2022JA030531

Young, D. T., Geiss, J., Balsiger, H., Eberhardt, P., Ghielmetti, A., & Rosenbauer, H. (1977). Discovery of He^{2+} and O^{2+} ions of terrestrial origin in the outer magnetosphere. *Geophysical Research Letters*, *4*(12), 561–564. https://doi.org/10.1029/GL004i012p00561

Yu, X., Yuan, Z., Wang, D., Li, H., Huang, S., Wang, Z., et al. (2015). In situ observations of EMIC waves in O^+ band by the Van Allen Probe A. *Geophysical Research Letters*, *42*(5), 1312–1317. https://doi.org/10.1002/2015GL063250

Yu, Y., & Ridley, A. J. (2013). Exploring the influence of ionospheric O^+ outflow on magnetospheric dynamics: Dependence on the source location. *Journal of Geophysical Research: Space Physics*, *118*(4), 1711–1722. https://doi.org/10.1029/2012JA018411

Yuan, Z., Xiong, Y., Huang, S., Deng, X., Pang, Y., Zhou, M., et al. (2014). Cold electron heating by EMIC waves in the plasmaspheric plume with observations of the Cluster satellite. *Geophysical Research Letters*, *41*(6), 1830–1837. https://doi.org/10.1002/2014GL059241

Yue, C., Ma, Q., Jun, C.-W., Bortnik, J., Zong, Q., Zhou, X., et al. (2020). The modulation of plasma and waves by background electron density irregularities in the inner magnetosphere. *Geophysical Research Letters*, *47*(15), e88855. https://doi.org/10.1029/2020GL088855

Zhang, X. J., Li, W., Thorne, R. M., Angelopoulos, V., Bortnik, J., Kletzing, C. A., et al. (2016). Statistical distribution of EMIC wave spectra: Observations from Van Allen Probes. *Geophysical Research Letters*, *43*(24), 12348–12355. https://doi.org/10.1002/2016GL071158

Zhou, Q., Xiao, F., Yang, C., He, Y., & Tang, L. (2013). Observation and modeling of magnetospheric cold electron heating by electromagnetic ion cyclotron waves. *Journal of Geophysical Research: Space Physics*, *118*(11), 6907–6914. https://doi.org/10.1002/2013JA019263

Zhu, H., & Chen, L. (2019). On the observation of electrostatic harmonics associated with EMIC waves. *Geophysical Research Letters*, *46*(24), 14274–14281. https://doi.org/10.1029/2019GL085528

Zhu, M., Yu, Y., & Jordanova, V. K. (2021). Simulating the effects of warm O+ ions on the growth of electromagnetic ion cyclotron (EMIC) waves. *Journal of Atmospheric and Solar-Terrestrial Physics*, *224*, 105737. https://doi.org/10.1016/j.jastp.2021.105737